City Research Online

City, University of London Institutional Repository

This is the accepted version of the paper.

This version of the publication may differ from the final published version.

Framework for Detection and Localization of Coronary Non-Calcified Plaques in Cardiac CTA using Mean Radial Profiles

Muhammad Moazzam Jawaid[a,*], Atif Riaz[a], Ronak Rajani[b], Constantino Carlos Reyes-Aldasoro[a], Greg Slabaugh[a]

[a]*City, University of London, Northampton Square, London, EC1V 0HB*
[b]*St Thomas' Hospital, Westminster Bridge Road, London, SE1 7EH*

Abstract

Background and Objective: The high mortality rate associated with coronary heart disease (CHD) has driven intensive research in cardiac imaging and image analysis. The advent of computed tomography angiography (CTA) has turned non-invasive diagnosis of cardiovascular anomalies into reality as calcified coronary plaques can be easily identified due to their high intensity values. However, the detection of non-calcified plaques in CTA is still a challenging problem because of lower intensity values, which are often similar to the nearby blood and muscle tissues. In this work, we propose the use of mean radial profiles for the detection of non-calcified plaques in CTA imagery.

Methods: Accordingly, we computed radial profiles by averaging the image intensity in concentric rings around the vessel centreline in a first stage. In the subsequent stage, an SVM classifier is applied to identify the abnormal coronary segments. For occluded segments, we further propose a derivative-based method to localize the position and length of the plaque inside the segment.

Results: A total of 32 CTA volumes were analysed and a detection accuracy of 88.4% with respect to the manual expert was achieved. The plaque localization accuracy was computed using the Dice similarity coefficient and a mean of 83.2% was achieved.

---

*Corresponding author
   Email address:* `muhammad.jawaid.2@city.ac.uk` (Muhammad Moazzam Jawaid)

Conclusion: The consistent performance for multi-vendor, multi-institution data demonstrates the reproducibility of our method across different CTA datasets with a good agreement with manual expert annotations.

1. Introduction

Coronary heart disease (CHD) is related to the accumulation of fatty materials (also termed as coronary plaques) inside coronary arteries. The growth of plaque leads to an obstruction of the vasculature that supplies blood to the heart musculature. Consequently, the heart muscles become oxygen starved which may result in fatal cardiac consequences including angina, heart failure and arrhythmias. According to the fact sheet of the World Health Organization [1], CHD was the leading cause of death globally in 2013, with 8.14 million deaths (16.8%) compared to 5.74 million deaths (12%) in 1990. Moreover, the recent statistics of the National Health Services, United Kingdom [2] reveals that over 2.3 million people in the United Kingdom suffer from CHD where the annual death toll is approximately 73,000 (an average of one death every seven minutes). The substantial levels of growing morbidity and mortality have led to a intensified interest in new techniques for detecting coronary abnormalities. From a clinical point of view, the detection and quantification of arterial plaque can help physicians avoid or at least delay the worst cardiac events by addressing behavioural risk factors [3].

The conventional methods used to detect coronary obstruction include catheter guided X-ray angiography, optical coherence tomography (OCT) and intravascular ultrasound (IVUS); however, their invasive nature make these methods time consuming and delicate due to considerable patient risk. In contrast, recent advancements in non-invasive imaging have improved the diagnostic accuracy in terms of high temporal and spatial resolution [4]. An example is the clinical use of cardiac computed tomography angiography (CTA) which enables precise

imaging of the heart with sub millimetre accuracy. This precision makes CTA a feasible alternative to cardiac catheterization for detecting coronary obstruction [5]; however, the composition of the coronary plaques pose a difficult challenge in the effective diagnosis.

Calcified plaques represent the deposition of calcium inside coronaries, whereas Non-calcified plaques are formed due to the presence of lipids and cholesterol. Clinically, the non-calcified plaques have been established as the most important indicator of acute coronary syndromes due to their fragile nature [6]. The risk of sudden rupture has made soft plaques threatening in clinical context, i.e. for many individuals, sudden death becomes the first sign of soft plaque in contrast to the calcified plaques which often lead to disease symptoms at early stages. Consequently, the intense focus of the current research is an early detection of soft plaques to predict and avoid worst cardiac events [7]. It should be noted that calcified plaques can be identified easily in a CTA image based on the high intensity value, consequently numerous methods have been reported with a reasonable detection accuracy [8, 9, 10, 11]. In contrast, the non-calcified plaques (NCP) usually have a lower intensity (similar to nearby heart tissues) that makes the detection problem challenging. Moreover, the positive remodelling associated with NCP (also termed as soft plaques) amplifies the detection challenge as the diameter-reduction based methods [8, 9, 10, 11, 12, 13] fail to detect the presence of soft plaques.

We now briefly summarize the flow of this paper. In Section 2 we review relevant literature addressing the CTA based soft plaque detection. Next, in Section 3 we briefly explain the clinical data used in this study. In Section 4 we explain the proposed model, whereas results are presented in Section 5. In Section 6, we provide concluding remarks and give directions for future research.

2. Related Work

Due to the complexity of the soft plaque detection problem, there is a little literature [14, 15, 16, 17, 18] published on automatic detection of soft plaques

in CTA imagery, out of which the majority have been clinical pilot studies or generic anomaly detection techniques. An automated framework was proposed by Clouse *et al.* [14] in which the main focus was the the quantification of manually identified soft plaques. From a dataset of 40 CTA volumes, a total of 49 coronary segments (41 normal, 8 abnormal) were investigated to validate the proposed quantification method. The results demonstrated that CTA based soft plaque quantification was possible; however the outcomes were based on a high degree of manual input i.e. selected coronary segments were investigated in the study. Moreover, the prior knowledge of plaque locations was an additional requirement as the quantification method required normal cross sections on terminal sites for computing the plaque volume. An extension of this pilot study reported successful correlation between CTA analysis and intravenous ultrasound (IVUS) plaque quantifications [19]. A total of 20 soft plaque effected segments were identified from 12 multi-detector CT (MDCT) volumes for comparative quantification. However, the main limitation of this work was the manual identification of plaque lesions that precludes an automated detection solution.

The use of machine learning in soft plaque detection was first reported by Wei *et al.* [15] where a linear discriminant analysis (LDA) was used to reduce the false positives in a set of 120 pre-selected soft plaque candidates. The accuracy of the classifier was mainly dependent upon NCP candidate selection criteria and machine learning was employed only to optimize performance by suppressing false candidates. A total of 120 plaque candidate regions were chosen from 83 CTA volumes in this study and a sensitivity of 92.5 percent was reported. Likewise, Tessman [18] proposed a learning based method for the classification of coronary stenosis. In the first step, the pre-extracted coronary centreline was used to map the vessel segment with a series of multi-scale overlapping cylinders to identify the sampling points inside the segment. In the following step, the authors extracted image based features at the sampled points including intensity, gradient magnitude, and the first order derivatives to detect the high intensity calcifications. Accordingly, the detection accuracies reported were 94% and 79%

4

respectively for the calcified and non-calcified plaques, along with a high number of false positives. The low detection accuracy for the soft plaques illustrate the fact that low-density based soft plaques demand a more sophisticated system i.e. beyond stenosis based computations to handle positive remodelling of the vessels.

Another interesting method for the automatic detection of vascular abnormalities was proposed by Zuluaga *et al.* [20]. In this work, the authors formulated a unsupervised learning system for detecting abnormal cross-sections in a vascular tube using "density level detection" technique of Steinwart [21]. Accordingly, the cross sectional images were discretely sampled around the tube centreline in first step to derive the feature set for discriminating outliers from normal cross sections. In the second step, an unsupervised SVM model trained on normal cross sections was used to detect the outliers i.e. the cross sections which violate the intensity pattern of normal class. The authors reported promising results for 9 clinical CTAs with NCP detection accuracy of 79.62%, however; the correct selection of ρ (parameter identifying the anomaly concentration) is important for the optimal results. Moreover, due to the one class unsupervised learning, a large number of normal cross sections with similar intensity pattern are required to train the SVM classifier, and the presence of nearby structure severely effects the classification performance.

Renard and Yang [16] proposed a computationally efficient method which integrated the plaque detection problem in the vessel segmentation framework. A coronary skeleton based on eigenvalue analysis was used to segment the lumen and vessel wall in the first stage. Soft plaques were detected in the second stage by comparing effective cross-sectional area of the lumen against vessel wall. Encouraging visual results were presented for this computationally efficient method, but no clinical validation was discussed in the paper. Moreover, the outcomes were reported for a very small data sample (2 CTA volumes only) which makes the reproducibility difficult. Lankton *et al.* [17] proposed a novel method in which the soft plaque detection was posed as an active contour segmentation problem. In this two stage detection process, the coronary tree was

extracted from the CTA volume in the first stage using mean separation energy model. In the subsequent step, two explicit surfaces derived from the original segmentation were evolved simultaneously to encompass low density soft plaques using the mean separation energy of Yezzi *et al.* [22]. A total of 8 CTA volumes were investigated and a detection rate of 88% against manual annotations was reported; however, a requirement for the careful initialization of evolving surfaces reduced the practicality of this method. One automated detection method was reported by Li *et al.* [23] in which region growing coronary segmentation was followed with voxel based detection analysis. In the plaque detection step, the authors constructed a voxel map of the vessel wall using morphological dilation and erosion. Subsequently, mean intensity at the internal and external interface of the vessel wall was computed and all the abnormal fluctuations were associated with soft plaques. However, no statistical data was provided for the detection rate in the paper.

In context of the non-calcified plaque quantification, a number of algorithms [24, 25, 26, 27] have been proposed in recent years with a motive of correlating CTA based plaque quantification with IVUS measurements. An innovative method for 3D reconstruction of coronary vasculature and arterial plaque quantification was proposed by Athanasiou *et al.* in [28]. In this work, authors used 4-class Gaussian Mixture Model to identify respective classes namely lumen, calcified plaque, non-calcified plaques and the background. In the subsequent step, the identified plaque voxels were reconstructed as surface mesh for comparison with IVUS segmentation. Accordingly, the paper reported efficiency over the existing literature and a good correlation with IVUS measurements;however, the blooming effect of calcified plaque resulted in relatively low agreement for calcified plaque volume.

Our contribution in this work is an efficient methodology for explicit detection and localization of the non-calcified plaques in clinical CTA. The first strength of this work is the use of discrete radial profiles in soft plaque detection. We demonstrate that the abnormal intensity drops resulting from soft plaque inside coronary vessels can be captured using concentric rings along the

vessel centreline. The second strength is the prototype of a machine learning framework for segregating non-calcified plaque affected coronary segments. In contrast to Wei *et al.* [15] where LDA was used to reduce the false positive rate, we directly employ a support vector machine (SVM) in our framework for segment-wise coronary classification.

The proposed model differs from the anomaly detection methods of [18, 20] that the coronary tree is segmented in the first stage using a hybrid energy model [29] which reveals radius variations along the length of vessels. Consequently, the radial information of the segment helps in tracing both positive and negative remodelling associated with the soft plaques. Furthermore, the plaque detection is performed using windowed statistics to uncover abnormalities in a relative context rather then evaluating individual cross sections as proposed in [20]. Experimental results demonstrate that the proposed method achieves a good agreement (detection accuracy of 88.4% with respect to manual annotations), and in-line with anomaly detection methods of [18], [20]. It should be noted that the explicit detection of the soft plaques is a challenging clinical problem. In this context, a number of local features proposed in [18] and [20] fails to detect the fragile low-intensity soft plaques; hence, the detection rate for the non-calcified plaques is significantly lower then the calcified plaque detections in [18] (i.e. 79.62% versus 94.05%).

In addition, the proposed model approximates the position and length of the non-calcified plaques in the abnormal coronary segment with a good accuracy of 83.24% against manual annotations. We believe that detected plaque terminal points can be used to design fully automated plaque quantification model in the future. For instance, Clouse's *et al.* [14] quantification can be automated using detected start and end positions.

3. Clinical Dataset Acquisition

Three different datasets have been studied for soft plaque detection in this work. The first dataset consisting of 18 CTA volumes has been downloaded from

7

publicly available database of Rotterdam Coronary Artery Evaluation framework [30, 31]. The Rotterdam CTA data comes from different sources and is based on different vendors as illustrated in Table 1. This multi-platform data

Table 1: Rotterdam CTA data specifications

Vendor	Siemens	Toshiba	Philips
Volume Count	6	6	6
Institution	Erasmus MC Uni.(NL)	Leiden Uni.(NL)	Utrecht Uni. (NL)
CT Scanner	Somatom Def.	Aquilion One 320	Brilliance 64
Slice/Rotation	32x2	320x1	64x1
ECG Gating	Retrospective	Retrospective	Retrospective
Kernel Used	b26f	b26f	b26f
Contrast Medium	Ultravist 370	Ultravist	Ultravist 370

makes the plaque detection problem challenging as a CTA volume reflects the acquisition dynamics; however, this serves as a great platform to ensure generalization of the proposed method. The motive behind using Rotterdam data is the availability of the manual ground truth in terms of expert annotations i.e. (normal/abnormal) and the precise position of soft plaque for the abnormal segments. A second dataset consisting of 12 CTA volumes is obtained from Guy's and St. Thomas' Hospital, London which was acquired using a Siemens Somatom Definition scanner. After obtaining the coronary centrelines, the orthogonal cross-sections were computed and an expert was requested to label the cross sections as normal or pathological (soft plaque affected). In addition, a third dataset consisting of two CTA volumes was obtained from Semmelweis university Budapest, Hungary and the segment wise orthogonal cross sections were annotated by manual expert as normal or soft plaque affected. Finally the manual annotations were validated with the help of clinical quantitative coronary angiography (QCA) report which was available for two datasets.

With a specific focus on the non-calcified plaque detection, the high intensity calcified plaques (if any) are generally pre-processed by assigning normalized

8

values to minimize the impact on non-calcified detection. This pre-processing was reported in [16, 32, 33] methods to optimize the detection process for non-calcified plaques. Similarly, plaque detection methods of [17, 15, 23] and quantification methods of [19, 14], started by suppressing the calcified plaque instances (if any) to ensure that the detection algorithm operates specifically on segments affected with the non-calcified plaques. Accordingly, we performed the normalization of the high intensity calcified plaques (if any) to stay within the scope of this non-calcified plaque detection work. However, it is important to mention that our proposed plaque detection method is robust to adapt the calcified plaque detections with a minor change is the detection principle, i.e. instead of isolating intensity dips, the intensity ascents or peaks are to be captured, and we aim to extend the current work for simultaneous processing of all types of plaques.

4. Proposed Model

In this work, we propose an efficient method for the detection and localization of soft plaques in clinical CTA. Accordingly, the segmentation of the coronary vasculature is performed in a first step using an improved formulation of Chan-Vese [34] energy model as defined in Jawaid *et al.* [29]. Next, we extracted the vessel centrelines from the segmented tree using sub-voxel thinning algorithm [35]. The accuracy of the obtained centrelines is evaluated by computing mean deviation error with respect to the reference ground truth as presented in Fig. 1. The visual comparison for complete coronary vasculature is presented in Fig. 1a, whereas the deviation error for individual segments (RCA, LCX, LAD and D1) is shown in Fig. 1b. It can be observed that the deviation error for the major coronary segments is less than one millimetre with respect to the reference centreline. In the subsequent step, we assigned a segment number to the individual coronary segments according to the 17-segment model of American Heart Association (AHA) [36], as the plaque detection is performed on per-segment basis. Next, the respective centrelines are used to extract the
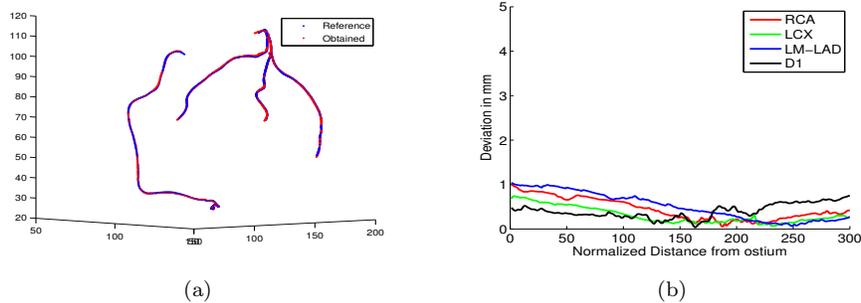
9

(a)   (b)

Figure 1: Accuracy of the coronary centreline with respect to the reference ground truth [31].(a) obtained centreline overlaid with the ground truth centreline, (b) mean deviation of the obtained centreline in millimeters. It can be observed that the coronary centreline has a mean deviation of about 1mm for the major segments.

orthogonal cross-sections to constitute the segment-wise cylindrical volume. In the following step, the support vector machine is applied to differentiate the plaque affected segments from the normal cross sections. The abnormal marked segments are investigated using second derivative analysis to identify the length and position of plaque inside coronary segments. For rest of the paper, we assume that I represents a CTA image and $\mathbf{x}$ is the spatial variable denoting 3D position in the domain Ω.

4.1. Mean Radial Profile

To investigate the intensity composition along the coronary segment, we employed the notion of the mean radial profile. We observed that this representation is effective to identify the intensity abnormalities in 3D tubular vessels by comparing radial profiles of successive 2D cross sections along the vessel axis. To illustrate the advantage of mean radial profiles, we obtained 2D cross sections along the length of segment by substituting respective centreline points in Eq. 1.

$$\mathbf{n} \cdot (\mathbf{x} - \mathbf{c}) = 0 \tag{1}$$

where $\mathbf{c}$ represents the centre of the plane and $\mathbf{n} = [n_x, n_y, n_z]^T$ represents the normal of the plane which is computed using successive points of the centreline
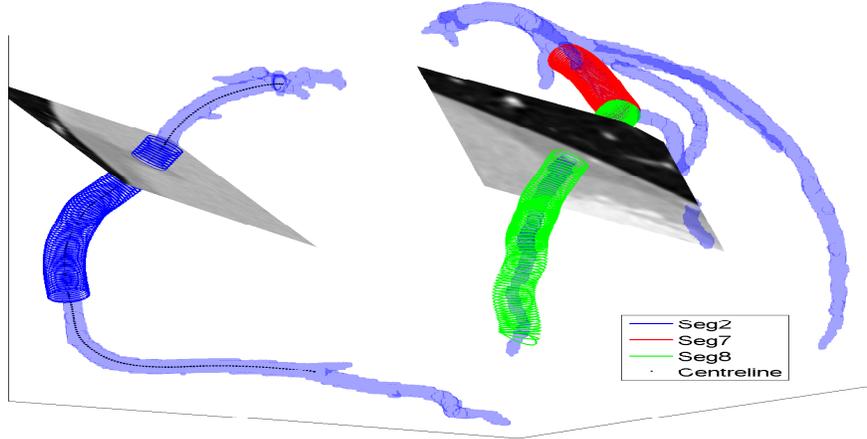
10

Figure 2: 3D segmented coronary trees with overlaid centreline and two cross sectional planes. The centreline is overlaid in black colour for the right coronary artery, whereas blue, red and green represents the curved cylindrical approximations for coronary segments numbered 2, 7 and 8 respectively. A local cylinder with 6mm diameter well encompasses the coronary segments.

to precisely follow the vessel orientation. In the subsequent step, we computed the respective radial profiles by sampling the obtained cross sections along concentric rings according to Eq. 2.

$$p[r, k] = \frac{\int_0^{2\pi} I(r, \theta, q_k) d\theta}{\int_0^{2\pi} d\theta} \tag{2}$$

where q denotes the segment centreline and q_k defines the k_{th} cross section of the centreline. Moreover, I represents the image intensity, r defines the radius, and θ defines the angle of a projecting ray. Fig. 3a shows the mean radial profiles for five sequential cross-sections (k=5, 10, 25, 40 and 45) of coronary segment. It should be noted that the intensity is maximum at the centre of a healthy cross section (i.e. k=5, 10, 40 and 45) and decreases outwards as a smooth function of distance. In contrast, the abnormal segments can be clearly differentiated based on an unexpected response of the mean radial profile. This deviation is visually illustrated in Fig. 3b where two cross-sections are displayed using optimal coronary display settings. High intensity in a normal cross section
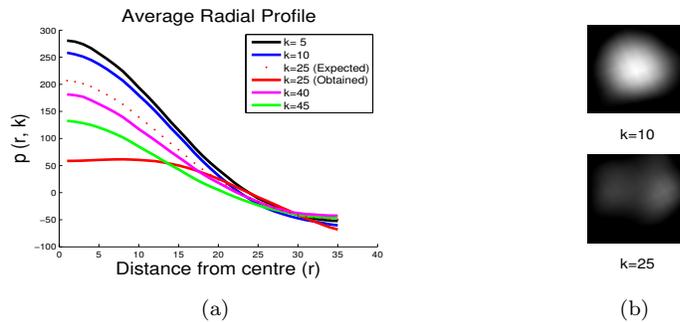
11

Figure 3: Mean radial profile based intensity examination to detect abnormality in 3D vessel. (a) show the radial profiles for five sequential cross sections to detect composition abnormality, whereas (b) shows 2 cross sections (normal and abnormal) at optimal display settings.

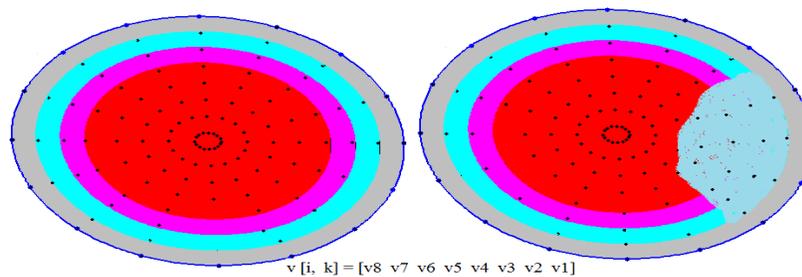$$v\,[i,\ k] = [v8\ \ v7\ \ v6\ \ v5\ \ v4\ \ v3\ \ v2\ \ v1]$$

Figure 4: Simulation of the intensity composition for normal and abnormal coronary cross sections. Left represents a normal cross section with adequate flow of blood, whereas right shows a plaque leading to blood obstruction. Moreover, the dots make the discrete radial profile obtained by sampling 8 concentric rings.

results in a bright appearance (top), whereas presence of low density material results in a darker appearance of the diseased cross section (bottom).

4.2. Cylindrical Modelling of Coronary Segments

To effectively use the radial profiles in plaque detection, we approximated the individual coronary segments with a curved cylindrical model having diameter of 6 mm. The choice of 6mm diameter is feasible as several studies [37], [12], [38] show that the maximum coronary diameter remains less than 6mm. Consequently, the circumference of our curved cylinder serves as exter-

nal boundary between the coronary vessel and background. This is illustrated in Fig. 2 where three different coronary segments are mapped with respective curved cylindrical models. This method of segment approximation is superior to Clouse *et al.*'s [14] approach, where a hard threshold of 0 Hounsfield units (HU) was used to cut off the vessel from the background. Nearby calcifications and image reconstruction artefacts often result in vessel borders that differ from 0 HU. Another advantage of our cylindrical approximation is that it allows a certain amount of flexibility in the centreline accuracy as the mean response of the 6mm region can successfully model the segment intensity distribution by overcoming the slight perturbations in the centreline. Next, we used the approximated curved cylindrical model of respective coronary segments to obtain the radial profiles. However, in context of the computational robustness, we used a discrete approximation of Eq. 2 to construct customized radial profiles along the length of segment. To maintain a trade-off between the computational load and the radial profile accuracy, the discretization parameters are chosen as $\Delta r = 0.4mm$, $\Delta\theta = 22.5°$ and $\Delta q = 0.4mm$. The sampling interval of 0.4 millimeters is used for the radial and cylindrical axis due to the isotropic voxel size, whereas an angular spacing of $22.5°$ is used to project 16 rays on the sampling plane. The chosen angular interval is fairly reasonable as the smaller interval leads to increased processing time without improving the performance. Accordingly, we define the customized radial profile as follows:

$$v[i,k] = \frac{1}{L}\sum_{t=1}^{L} I(r_i, \theta_t, q_k) \,\forall i, k, \; i = 1, ..., 8, \; k = 1, ...K \tag{3}$$

where q_k represents the kth cross sectional of coronary segment and K defines the total number of points along the length of the segment. L denotes the total number of projected rays, which is set equal to 16 in our model and the respective projection angle is computed as $\theta_t = t\left(\frac{\pi}{8}\right)$. Moreover, i denotes the concentric ring formed at radius $r_i = 0.4(9-i)$mm. This formulation of r_i reveals that the outermost ring is labelled as v_1 and the innermost ring is denoted as v_8. Moreover, this discrete approximation is illustrated in context of two cross sections in Fig. 4 where it is apparent that the outer four rings (v_1

to v_4) generally defines the interface between lumen and external fat, while the inner four rings (v_5 to v_8) represent the contrast medium affected blood.

This fact is further demonstrated in Fig. 5 where the intensity response of eight concentric rings is plotted for the complete segment. It can be observed that irrespective of the segment composition, the inner four rings reflect the impact of the contrast medium in terms of high intensity, whereas the outer four rings represent comparatively lower HU values related with external boundary of the vessel. Moreover, Fig. 5 shows that the healthy segments lead to stable intensity response for all the eight rings (see Fig. 5a) throughout the segment length, whereas the presence of low intensity (soft plaques) results in significant concavities for inner four rings (see Fig. 5b). We observed that this considerable disparity in the stability of four inner rings can be used to differentiate coronary segments into two classes i.e. normal and abnormal. Consequently, we derived the mean representation (s) of the coronary segments by averaging the response of four inner rings as expressed in Eq. 4. It should be noted that the segment mean representation s is based on four inner rings, which minimizes the probability of erroneous plaque detection associated with 6 mm circular approximation of distal segments.

$$s[k] = \frac{1}{4} \sum_{i=5}^{8} v[i, k], \ \forall k, \ k = 1...K \tag{4}$$

To overcome the short term fluctuations in the mean representation of the coronary segments, we applied finite impulse response filter using a moving window technique. Accordingly, the smoothed statistical representation of the coronary segment is obtained with the help of moving mean and moving standard deviation operation as expressed in Eq. 5, where n i.e. the size of moving window is set equal to 3.

$$\sigma_s[k] = \sqrt{\frac{1}{(2n+1) - 1} \sum_{i=-n}^{n} (s[k+i] - \mu[k])^2},$$

$$\mu_s[k] = \frac{1}{2n+1} \sum_{i=-n}^{n} s[k+i], \ \forall k, \ k = 1, ..., K \tag{5}$$

14
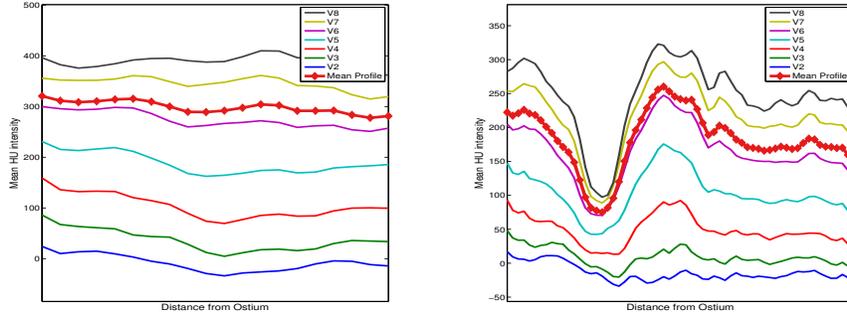
(a) CTA Volume 6 Segment 1 (normal). (b) CTA Volume 4 Segment 2 (abnormal)

Figure 5: Mean intensity response for 8 concentric rings (v_1 to v_8) along the length of segment. The mid of the lumen, (v_8) exhibits high HU intensity, whereas a low value of (v_1) indicates a position away from the lumen centre. Moreover, the mean profile of the coronary segment is obtained by averaging the four inner rings (v_8) - (v_5).

In addition, we constructed the segment radius profile S_{rad} by computing the lumen radius from the segmented coronary tree to take into account the remodelling impact along the length of the vessel. It should be noted that different coronary segments have variable length as defined in standard AHA coronary model (see Fig. 2 for visual difference between segment 2, segment 7 and segment 8). We apportioned the variable length of individual segments at this stage with the help of spline interpolation to redefine the segments in terms of the fixed length characteristic functions μ'_s, σ'_s and S'_{rad} (each having 100 samples).

4.3. SVM Based Segment Classification

4.3.1. Feature Based Representation for Coronary Segments

After obtaining the fixed length characteristic functions for coronary segments, we used an SVM classifier to differentiate the plaque affected segments from the normal ones. An imperative pre-requisite for a learning-based classifier is the selection of appropriate features from the data. Ambiguous features failing to discriminate two classes effectively leads to poor accuracy, whereas distinctive features result in optimal classification. It should be noted that the
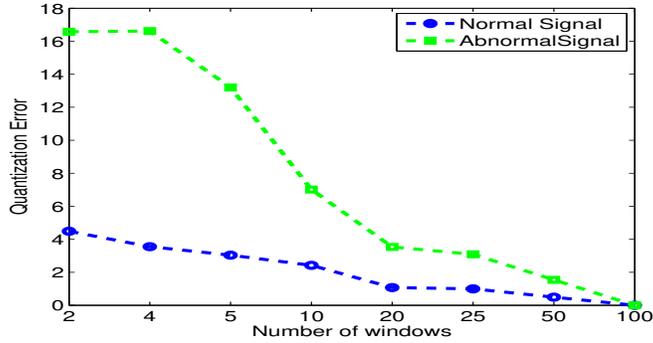
15

Figure 6: Subset based signal representation to reduce the dimensions of the feature vector. It can be observed that both (normal and abnormal) classes can be adequately represented using 20 subsets.

non-calcified plaques can be optimally detected by investigating the composition of the arterial segment. Hence intensity based features play an important role in the abnormality detection process. Moreover, non-calcified plaques generally lack a specific texture or shape which makes the application of geometric features relatively difficult. Recent clinical studies [39, 40] have shown that Napkin Ring Sign (NRS) can be used as a shape descriptor; however, it is applicable on significantly developed stable non-calcified plaques. Accordingly, we identified the representative features of our data by analytical investigation before applying the SVM model to ensure the computational robustness. As the motive of this work is to detect plaque-based abnormalities along the length of the segment, we therefore extracted the features by splitting the characteristic functions $\mu_s^{'}$ and $\sigma_s^{'}$ into m windows as expressed in Eq. 6.

$$f_\mu[m] = \sum_{n=1}^{5} \mu_s^{'}[n + 5(m - 1)], \forall m = 1, 2, ..., 20$$

$$f_\sigma[m] = \sum_{n=1}^{5} \sigma_s^{'}[n + 5(m - 1)], \forall m = 1, 2, ..., 20 \tag{6}$$

The windowed or sub-set based statistics can effectively reveal the relative changes along the length of segment; however, the selection of m is critical as it serves as a trade-off between the the approximation error and the feature

16

(a) Normal windowed mean.

(b) Abnormal windowed mean.

(c) Normal windowed Std.
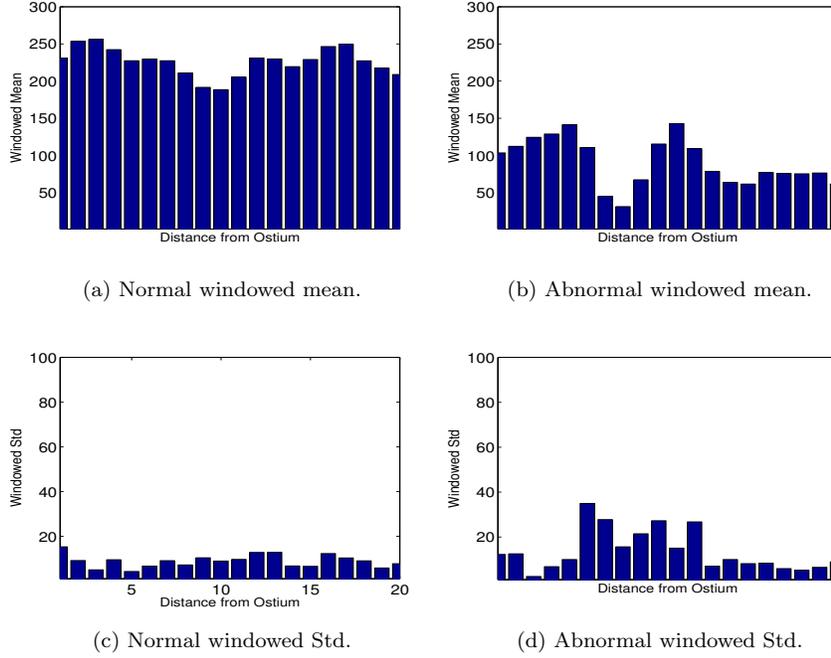
(d) Abnormal windowed Std.

Figure 7: Graphical representation for segment representative features. (a, c) defines a normal segment having stable mean and deviation, whereas (b, d) represents a soft plaque effected segment.

vector dimensions. To select the optimal number of windows, we investigated the relation between m and segment approximation accuracy as shown in Fig. 6. It can be observed that the quantization error is inversely proportional to the number of windows, i.e. increase in m leads to improved approximation of the segment profile s. Thus, to maintain a balance between the accuracy and the feature vector size, we defined number of windows m equal to 20. The choice of 20 windows is reasonable, as both normal and abnormal segments show that the approximation error becomes steady at $m = 20$. Fig. 7 demonstrates the discriminative capability of extracted features (f_μ and f_σ) to distinguish the intensity patterns of two classes (see Fig. 7a - 7d).

Furthermore, two additional parameters namely mid-lumen intensity f_{mid} and mean radius f_{rad} are added to improve the performance of the SVM clas-

sifier. The mid-lumen intensity through the vessel is acquired by modelling the intensity response of the innermost ring v_8 through the length of vessel as expressed in Eq. 7, whereas the mean radius f_{rad} encoding the vessel remodelling impact is approximated in terms of m windows using radial profile S'_{rad} as expressed in Eq. 8.

$$f_{mid}[m] = \frac{1}{5}\sum_{n=1}^{5} v_8[n + 5(m-1)], \forall m = 1, 2, ..., 20 \qquad (7)$$

$$f_{rad}[m] = \frac{1}{5}\sum_{n=1}^{5} S'_{rad}[n + 5(m-1)], \forall m = 1, 2, ..., 20 \qquad (8)$$

Fig. 9a - 9d demonstrate the advantage of the additional features. Apparently f_{mid} replicates the distribution pattern of f_μ; however, it encodes the mid-lumen behaviour (i.e. the concentration of the contrast medium) from ostium to the end of segment. It should be noted that a plaque present in the segment ostium (or even in the preceding segment) will result in low HU intensity through the mid of lumen; hence, the segment should be classified as abnormal but the stable mean and variance may lead to an erroneous classification in terms of normal region. In this context, the feature f_{mid} ensures that the classifier takes into account not only the intensity variations but the mid-lumen response of segment for efficient classification.

Motivation for using the radius based feature f_{rad} is illustrated in Fig 8. It can be observed from the figure that the vessel boundary (red contours) suffer through compressions at three distinct points along the length. The compression points represent stenosis locations of different degrees (mild, mild, moderate) respectively. The impact of the vessel stenosis can be clearly visualized in terms of the vessel radius f_{rad} plotted in blue colour, as the radius shows an unexpected dip in the stenosis region. In general, the radius obtained along the length of the segment conveys useful information to the classifier regarding vascular abnormality as illustrated in Fig. 9c - 9d. It can be observed from Fig. 9c that the segment radius decreases smoothly as a function of ostia distance for normal segment, whereas the plaque effected regions undergo unexpected variations in
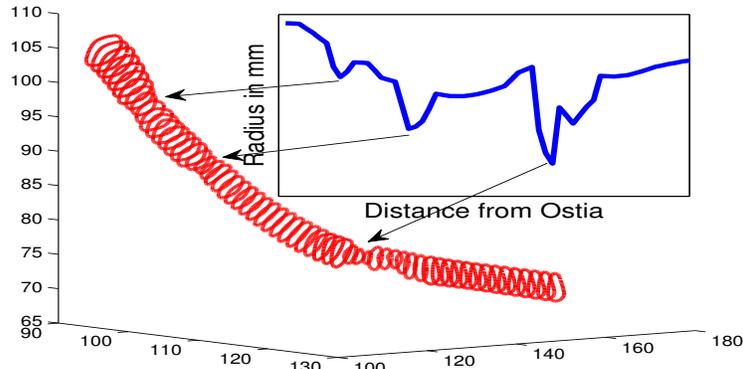
18

Figure 8: 3D boundary contours (red) for segmented coronary vessel and corresponding radius(blue).Three stenotic locations in the vessel are well reflected in radius deviations.

radii due to the positive or negative remodelling in the plaque affected area. The statistical results illustrate that integration of the mid lumen intensity and the segment radial information improves the classifier accuracy by approximately 11% as demonstrated in Section 5. Next, we concatenate four feature sets f_μ, f_σ, f_{mid} and f_{rad} to obtain a feature based representation $\mathbf{Fx}_i$ for respective coronary segment with dimensions [1 x 80].

4.3.2. Feature Selection Methods

Based on the fact that we employed prior clinical knowledge to derive hand-crafted features in the context of non-calcified plaque detection, it is less likely that feature selection techniques will significantly reduce the dimensionality of the feature space. For the proof of concept, we compared three different feature selection techniques including Relief-F [41], recursive feature elimination [42] and Fisher [43] methods using a feature selection library [44]. To illustrate the efficiency of these methods we performed the classification using top ranking features for three techniques as shown in Fig. 10. It can be observed that use of the top 5 features leads to a minimal accuracy for all three techniques, whereas an increased feature space lead to a continuous improvement in the accuracy
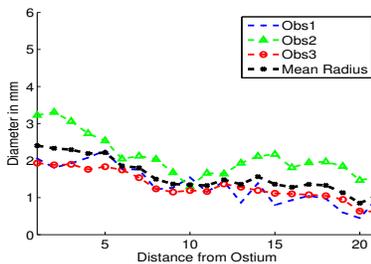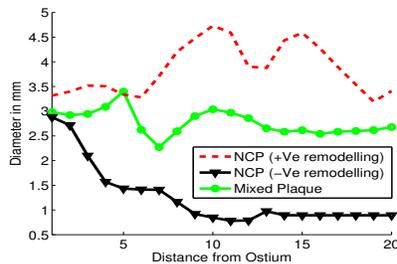
19
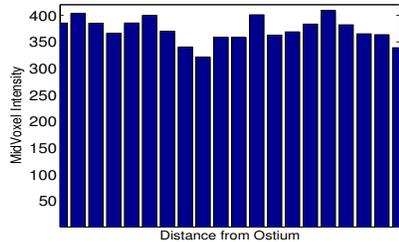
(a) Normal mid voxel intensity.
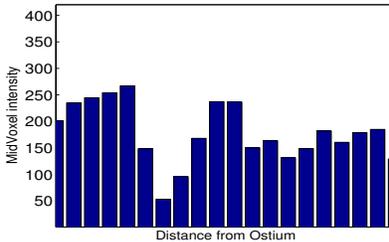
(b) Abnormal mid voxel intensity.

(c) Normal radius pattern

(d) Abnormal radius pattern

Figure 9: Graphical representation for segment representative features. (a, c) defines mid-lumen intensity and radius trend for normal segments, whereas (b, d) represents the abnormal segment. It can be observed that normal segments are characterized with high mid-lumen intensity and smooth decreasing radius, whereas abnormal segment is related with low mid-lumen intensity and often suffers with unexpected radius variations (+ve, -ve and hybrid vessel remodelling).

of the classifier. This is due to the window-based nature of the features as increased windowed statistics allow the classifier to make relatively improved decision. From a comparative point of view, it can be observed from Fig. 10 that the Fisher method [43] achieves higher accuracy as it employs the correlation information to to rank the feature's discriminative power.

4.3.3. SVM Classification Framework

For an SVM based classification, our data consists of n feature vectors of the form $\mathbf{Fx}_i$ and the associated binary labels y_i defining the class of vector as normal or diseased. The mathematical representation for classification data is
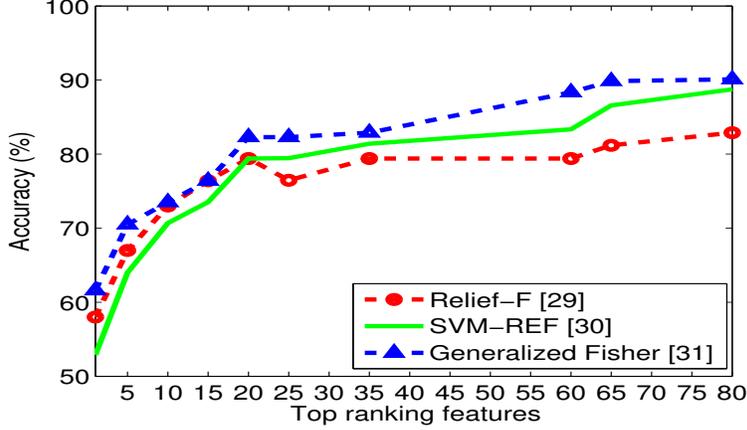
20

Figure 10: Classification accuracy based on top ranking features for three different feature selection techniques. Method [43] shows comparatively better accuracy due to correlated feature information.

as follows:

$$D = \left\{ (\mathbf{F}\mathbf{x}_i, y_i) \, | \mathbf{F}\mathbf{x}_i \subseteq R^d, y_i \subseteq \{-1, 1\} \right\}_{i=1}^{n} \tag{9}$$

where n is the number of samples, and d denotes the feature vector dimension i.e set equal to 80 in our work. The use of support vector machines in binary classification is equivalent to quadratic optimization subject to linear constraints. The SVM model finds an optimal hyperplane by minimizing the norm of weights for ideal segregation; however, a slack variable is often integrated to relax the constraints for a feasible solution as expressed in Eq. 10.

$$min \, |\mathbf{w}|^2 + P \sum_{i=1}^{n} \varepsilon_i \tag{10}$$

$$subject \, to : y_i \left(\mathbf{w}^T \mathbf{F}\mathbf{x_i} + b \right) \geq 1 - \varepsilon_i, \, \varepsilon_i \geq 0, for \, i = 1, 2, ...n$$

A penalty cost P regulates the influence of individual support vectors in the classification as high value of P leads to hard margin, whereas very small value allows frequent violations of the constraints. After investigating values in the interval $\left[10^{-5}, 10^5 \right]$, we defined $P = 10^0$ by adjusting the box-constraint parameter of the SVM classifier. Moreover, we used a non-linear radial basis Gaussian

21

kernel for mapping data into higher space with sigma defined equal to 1. Accordingly, the SVM model classifies the test vector $\mathbf{Fx_i}$ into normal or diseased class according to Eq. 11.

$$Out\left(\mathbf{Fx}_i\right) = sgn\left(\mathbf{w}^T\mathbf{Fx}_i + b\right) \tag{11}$$

4.4. Plaque Localization in Abnormal Segment

Segments classified as "abnormal" are further investigated for precise position of the plaque in the vessel. The essence of localization process is to identify unpredicted intensity dips in the mean radial profile of the coronary segment. For tracking valleys in the mean profile (s) of an abnormal segment, we computed the intensity variation enormity using a first order derivative. It should be noted from Fig. 11 that the relative slope (shown in blue colour) remains steady through the normal regions of the coronary segment, whereas the unexpected drop associated with soft plaques lead to a significant transition in the slope magnitude. In the subsequent step, we applied second order derivative analysis of Eq. 12 to identify the local extrema points. This computation is based on the idea that valley region can be well characterized by pair of adjacent maxima points as shown in Fig. 11.

After identifying the local extrema positions, we quantified the section-wise intensity drop by computing the sum of relative slope between successive maxima points. Consequently, two maxima encompassing the maximal intensity drop are marked as the start and end positions of the lesion in the segment. To generalize the performance, an additional constraint was posed directly in terms of an intensity threshold of 50 HU to ensure that low HU value inside the vessel were directly marked as plaque without requiring any additional evidence.

$$f''\left(s\right) = \begin{cases} Maxima\ at\ \left(s=p\right)\ \text{if}\ f'\left(s\right)=0\ \&\ \frac{\partial^2 f}{\partial s^2} > 0 \\ Minima\ at\ \left(s=p\right)\ \text{if}\ f'\left(s\right)=0\ \&\ \frac{\partial^2 f}{\partial s^2} < 0 \end{cases} \tag{12}$$
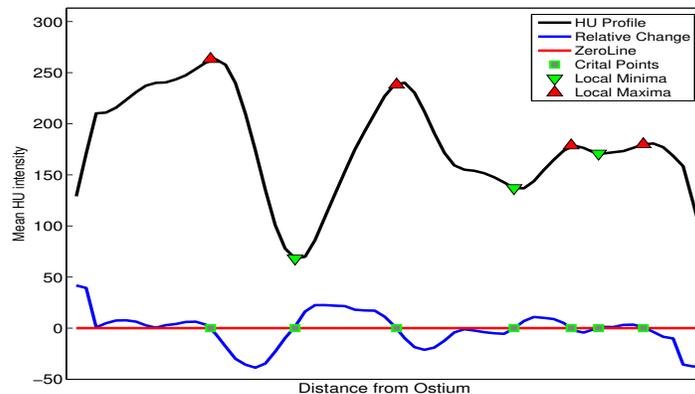
22

Figure 11: Derivative based plaque localization in an abnormal segment. Black represent segment mean profile and blue curve show the relative change in mean profile. Moreover, red and green markers show the detected local extrema points.

5. Results

5.1. Results for SVM Classification

Out of the available 32 CTA volumes, a total of 344 segments (200 normal, 144 abnormal) are extracted in the first stage for validation of the SVM classifier. In the subsequent stage, the mean HU profiles are generated as defined in Section 4 for individual coronary segments. The performance of our SVM classifier is presented in Fig. 12 where Leave One Out (LOO) cross-validation shows promising results with a sensitivity of 93%. Furthermore PPV for the LOO validation is 86.4% and NPV is 91.9% which makes the overall soft plaque detection accuracy equal to 88.4%.

Next, we used the trained SVM classifier to investigate the impact of feature vector dimensions on the classifier efficiency. In this test we used 122 coronary segments extracted from 3 datasets (70 normal and 52 abnormal according to the manual ground truth) and compared the classifier performance in terms of accuracy and processing time. It has been observed that the windowed mean and deviation based 40 features lead to a classification accuracy of 77.8%, where
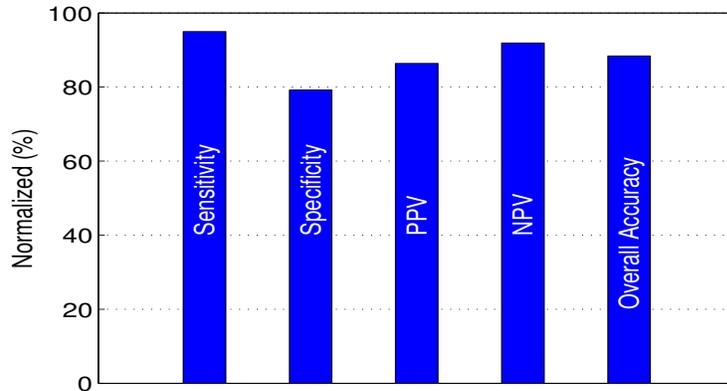
23

Figure 12: Leave One Out validation for the SVM classifier. The overall accuracy (around 88.4%) shows the effectiveness of the plaque detection method.

the addition of mid-lumen f_{mid} and radius f_{rad} based features improved the classifier accuracy by approximately 11%. Moreover, the comparative analysis demonstrates that the further increase in the feature space dimensions show only a marginal improvement in the classifier accuracy, while the computational time increases significantly. These results lead to the conclusion that the classifier performance becomes resistant to the feature vector dimensions at a certain point due to the redundancy of features.

We evaluated the efficiency of our classification model against three individual datasets to validate the reproducibility on generic CTA data. We extracted test segments individually from three datasets (66 from Rotterdam, 76 from St. Thomas and 36 from Semmelweis) and SVM classification results are presented in Fig. 13. It should be noted that the individual classification accuracy is consistent around 85% across the data. Moreover, the classification results of Fig. 13 can be interpreted based on the fact that a "significant intensity dip" helps the classifier to achieve higher accuracy. In this context, the high sensitivity of the Rotterdam data can be related with the presence of severe soft plaques in different coronary segments, whereas the lower accuracy for Semmelweis CTA dataset reflects less test data and the absence of severe plaque instances. It
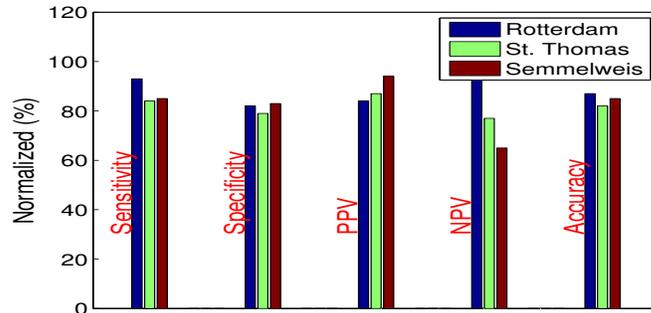
24

Figure 13: Plaque detection results for three individual datasets using individual statistics and overall accuracy. It can be observed that SVM consistently achieves plaque detection rate higher than 80%.

should be noted that the detection of the immature (clinically graded as mild to moderate) soft plaque becomes extremely difficult due to uncertain intensity profiles.

5.2. Results for Plaque Localization

SVM based identification of the abnormal segments is followed by the localization of the plaque inside the vessel. The plaque localization is illustrated in Fig. 14 where first and second order derivative analysis is used to highlight the intensity concavities. The proposed model achieved encouraging results as all substantial plaques are well localized; however, it slightly overestimates the plaque position due to numerical dependence on the second order extrema points as shown in Fig. 14. The accuracy for plaque localization is evaluated by computing the Dice similarity index between the ground truth and the detected plaque locations. The total number of cross sections along the segment are represented using a binary vector where a *zero* denotes normal cross section and *one* reflects the abnormality. The ground truth vector is constructed using the start and end positions of the soft plaque from the manual observer annotations, whereas the obtained plaque vector is derived from our detected plaque positions.
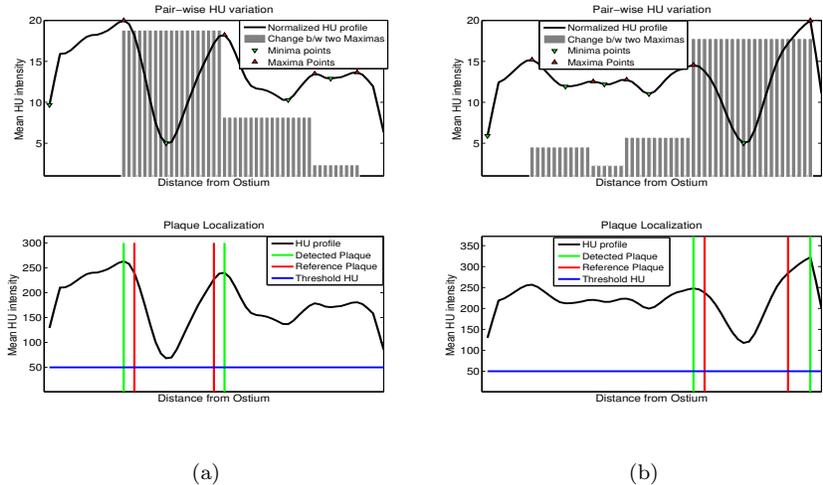
25

Figure 14: Plaque localization for abnormal segments of Rotterdam data (Green is detected region and red is the manual ground truth). It can be observed that the proposed method identifies the plaque region in the vessel with a slight over-estimation. First row shows the section-wise first order change between consecutive maxima pairs, whereas the second row shows detected plaque region.

Fig. 15a demonstrates the efficacy of the plaque localization method with a mean Dice index of 83.2% with respect to the expert annotations. Moreover, Fig. 15a also presents the plaque length in millimeters where our obtained length is in correlation with the expert based length. However, a trend of slight over-estimation can be observed which is due to the numerical dependence on second derivative-based maxima points. The shortcoming of the plaque localization method can also be observed in Fig. 15a as plaque length and Dice index under performs for CTA volume 6 and 15. The mismatch for these two volumes occurred due to the unexpected length of the plaque (spanning over the complete segment) that leads clinician to make a relative decision. This is further illustrated in Fig. 15b, where the human observer selected start and the end positions of the plaque relative to the significant intensity drop and the complete intermediate region is marked as plaque, whereas the proposed model results in two individual plaque instances centred at the start and the end of
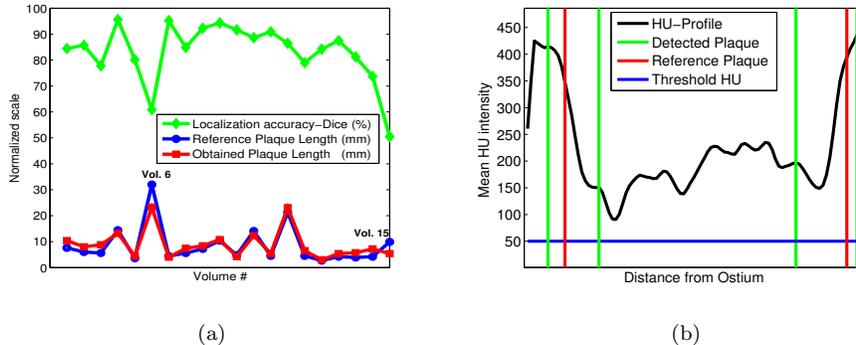
26

Figure 15: Plaque localization performance. (a) show the localization accuracy using Dice index (%) and the plaque length with respect to the manual expert of Rotterdam, (b) show a particular case where the proposed method fails in precise localization of plaque.

the actual plaque.

6. Discussion

We proposed a simple yet efficient method for detection of the non-calcified coronary plaques using support vector machines. The innovative aspect of this work includes automated detection of the abnormal coronary segments (affected with non-calcified plaques) using SVM classifier. Moreover, this model precisely locates the position and approximate length of the non-calcified plaque in abnormal segment which can be used in fully automated plaque quantification. The overall accuracy of our plaque detection model is 88.4% against the manual observer ground truth with a sensitivity of 93% and specificity of 80%. Moreover, the Dice coefficient for plaque localization in diseased segments is 83.2% with respect to clinical annotations. Moreover, the proposed model has been tested on three different CTA datasets individually and has produced consistent results, demonstrating its reproducibility for generic CTA data.

After comparing individual results, we also compared our outcome with plaque detection models of Wei *et al.* [15], Lankton *et al.* [17] and Tessmann *et al.* [18] to establish a correlation with the reported literature. It should be

27

noted that the overall detection trend can be observed in Table 2 for different methods; however, a head to head comparison is not possible with [15] and [17] as the results are based on different quantitative metrics. For instance, the sensitivity reported by Lankton *et al.* [17] is achieved using volume based processing, whereas Wei *et al.* [15] used 2mm long plaque candidate regions.

Table 2: Plaque detection - Comparison with reported methods.

	Proposed	Tessman[18]	Lankton[17]	Wei[15]
Test Volumes	32	45	8	83
Classifier	SVM	AdaBoost	Energy Minimization	LDC
Target Plaques	Non-calcified	Non-calcified	Non-calcified	Non-calcified
Features Used	80	144	x	14
Data set Tested	User Defined	User Defined	User Defined	User Defined
Detection Target	Coronary segments	Coronary segments	Plaque regions	Plaque candidates
Sensitivity	93	79.62	88	92

The limitations of this work include an under-estimation of the long plaques in fully occluded segments and the low detection rate for the minor coronary segments due to the reduced diameter. However, from a clinical point of view, the plaques present in the minor segments are less threatening as they do not cause sudden fatalities due to limited muscular damage. The future work on this method will include manual input from multiple experts to investigate the classifier efficiency relative to inter-observer error. Moreover, an ongoing study is extending this work in which we aim to perform a quantitative analysis for localization accuracy and aggregate plaque volume in the coronary tree. Another possible extension of the current work can be replacement of the hand-crafted features with a convolutional neural network (CNN) to take maximal advantage of machine learning procedures; however, this requires a large repository of CTA data.

7. Conclusion

The proposed automated non-calcified plaque detection method shows a good detection rate of 88.4% and plaque localization accuracy of 83.2% with respect to manual ground truth. Moreover, we compared our results with earlier studies and found a good agreement with abnormality detection rate of Wei *et al.* [15], Lankton *et al.* [17] and Tessmann *et al.* [18]. We believe this can serve as an important step forward towards the automated quantification of the soft plaques, which have been identified as the major reason of fatal cardiac events.

References

[1] S. Waxman, F. Ishibashi, J. E. Muller, Global, regional, and national age-sex specific all-cause and cause-specific mortality for 240 causes of death, 1990-2013: a systematic analysis for the global burden of disease study 2013, Lancet 385 (9963) (2015) 117–171.

[2] U. K. NHS, Coronary Heart Disease, statistics for united kingdom, Available at `http://www.nhs.uk/Conditions/Coronary-heart-disease/Pages/Introduction.aspx`(2016/11/11).

[3] W. H. Organization, Cardiovascular diseases CVDs, the global statistics, Available at `http://www.who.int/mediacentre/factsheets/fs317/en/`(2016/11/11).

[4] T. Flohr, B. Ohnesorge, Multi-slice ct technology, in: Multi-slice and Dual-source CT in Cardiac Imaging, Springer, 2007, pp. 41–69.

[5] M. S. David C. Levin, D. Fischman, Coronary CTA, a cost-effective alternative to cardiac catheterization for the evaluation of cad, study suggests, Available at `https://www.sciencedaily.com/releases/2010/04/100421162617.htm`(2016/12/07).

[6] R. Virmani, A. P. Burke, A. Farb, F. D. Kolodgie, Pathology of the vulnerable plaque, Journal of the American College of Cardiology 47 (8s1) (2006) C13–C18.

[7] S. Waxman, F. Ishibashi, J. E. Muller, Detection and treatment of vulnerable plaques and vulnerable patients novel approaches to prevention of coronary events, Circulation 114 (22) (2006) 2390–2411.

[8] S. C. Saur, H. Alkadhi, L. Desbiolles, G. Székely, P. C. Cattin, Automatic detection of calcified coronary plaques in computed tomography data sets, in: International Conference on Medical Image Computing and Computer-Assisted Intervention, Springer, 2008, pp. 170–177.

[9] G. Brunner, U. Kurkure, D. R. Chittajallu, R. P. Yalamanchili, I. A. Kakadiaris, Toward unsupervised classification of calcified arterial lesions, in: International Conference on Medical Image Computing and Computer-Assisted Intervention, Springer, 2008, pp. 144–152.

[10] I. Išgum, A. Rutten, M. Prokop, B. van Ginneken, Detection of coronary calcifications from computed tomography scans for automated risk assessment of coronary artery disease, Medical physics 34 (4) (2007) 1450–1461.

[11] B. Mohr, S. Masood, C. Plakas, Accurate lumen segmentation and stenosis detection and quantification in coronary cta, in: Proceedings of 3D Cardiovascular Imaging: a MICCAI segmentation challenge workshop, 2012.

[12] R. Shahzad, H. Kirisli, C. Metz, H. Tang, M. Schaap, L. van Vliet, W. Niessen, T. van Walsum, Automatic segmentation, detection and quantification of coronary artery stenoses on cta, The International Journal of Cardiovascular Imaging 29 (8) (2013) 1847–1859.

[13] R. Shahzad, L. van Vliet, W. Niessen, T. van Walsum, Automatic classification of calcification in the coronary vessel tree, Available at `http://orcascore.isi.uu.nl/wp-content/uploads/2014/09/BIGR_CaSc.pdf`(2016/11/11).

30

[14] M. E. Clouse, A. Sabir, C.-S. Yam, N. Yoshimura, S. Lin, F. Welty, P. Martinez-Clark, V. Raptopoulos, Measuring noncalcified coronary atherosclerotic plaque using voxel analysis with mdct angiography: a pilot clinical study, American Journal of Roentgenology 190 (6) (2008) 1553–1560.

[15] J. Wei, C. Zhou, H.-P. Chan, A. Chughtai, P. Agarwal, J. Kuriakose, L. Hadjiiski, S. Patel, E. Kazerooni, Computerized detection of noncalcified plaques in coronary ct angiography: Evaluation of topological soft gradient prescreening method and luminal analysis, Medical Physics 41 (8) (2014) 081901.

[16] F. Renard, Y. Yang, Image analysis for detection of coronary artery soft plaques in mdct images, in: 5th IEEE International Symposium on Biomedical Imaging: From Nano to Macro, IEEE, 2008, pp. 25–28.

[17] S. Lankton, A. Stillman, P. Raggi, A. Tannenbaum, Soft plaque detection and automatic vessel segmentation, in: 12th International Conference on Medical Image Computing and Computer Assisted Intervention (MICCAI), Springer Berlin Heidelberg, 2009, pp. 25–33.

[18] M. Tessmann, F. Vega-Higuera, D. Fritz, M. Scheuering, G. Greiner, Multiscale feature extraction for learning-based classification of coronary artery stenosis, in: SPIE Medical Imaging, International Society for Optics and Photonics, 2009, pp. 726002–726002.

[19] H. Brodoefel, C. Burgstahler, A. Sabir, C.-S. Yam, F. Khosa, C. D. Claussen, M. E. Clouse, Coronary plaque quantification by voxel analysis: dual-source mdct angiography versus intravascular sonography, AJR. American Journal of Roentgenology 192 (3) (2009) W84.

[20] M. A. Zuluaga, I. E. Magnin, M. H. Hoyos, E. J. D. Leyton, F. Lozano, M. Orkisz, Automatic detection of abnormal vascular cross-sections based on density level detection and support vector machines, International Journal of Computer Assisted Radiology and Surgery 6 (2) (2011) 163–174.

31

[21] I. Steinwart, D. R. Hush, C. Scovel, Density level detection is classification., in: NIPS, 2004, pp. 1337–1344.

[22] A. Yezzi, A. Tsai, A. Willsky, A fully global approach to image segmentation via coupled curve evolution equations, Journal of Visual Communication and Image Representation 13 (1) (2002) 195–216.

[23] Y. Li, W. Chen, K. Liu, Y. Wu, Y. Chen, C. Chu, B. Fang, L. Tan, S. Zhang, A voxel-map quantitative analysis approach for atherosclerotic noncalcified plaques of the coronary artery tree, Computational and Mathematical Methods in Medicine 2013.

[24] S. Achenbach, F. Moselewski, D. Ropers, M. Ferencik, U. Hoffmann, B. MacNeill, K. Pohle, U. Baum, K. Anders, I.-k. Jang, et al., Detection of calcified and noncalcified coronary atherosclerotic plaque by contrast-enhanced, submillimeter multidetector spiral computed tomography, Circulation 109 (1) (2004) 14–17.

[25] A. W. Leber, A. Becker, A. Knez, F. von Ziegler, M. Sirol, K. Nikolaou, B. Ohnesorge, Z. A. Fayad, C. R. Becker, M. Reiser, et al., Accuracy of 64-slice computed tomography to classify and quantify plaque volumes in the proximal coronary system, Journal of the American College of Cardiology 47 (3) (2006) 672–677.

[26] T. Schepis, M. Marwan, T. Pflederer, M. Seltmann, D. Ropers, W. G. Daniel, S. Achenbach, Quantification of non-calcified coronary atherosclerotic plaques with dual-source computed tomography: comparison with intravascular ultrasound, Heart 96 (8) (2010) 610–615.

[27] M. Otsuka, N. Bruining, N. C. Van Pelt, N. R. Mollet, J. M. Ligthart, E. Vourvouri, R. Hamers, P. De Jaegere, W. Wijns, R. T. Van Domburg, et al., Quantification of coronary plaque by 64-slice computed tomography: a comparison with quantitative intracoronary ultrasound, Investigative radiology 43 (5) (2008) 314–321.

[28] L. Athanasiou, G. Rigas, A. I. Sakellarios, T. P. Exarchos, P. K. Siogkas, C. V. Bourantas, H. M. Garcia-Garcia, P. A. Lemos, B. A. Falcao, L. K. Michalis, et al., Three-dimensional reconstruction of coronary arteries and plaque morphology using ct angiography–comparison and registration with ivus, BMC medical imaging 16 (1) (2016) 9.

[29] M. M. Jawaid, R. Rajani, P. Liatsis, C. C. Reyes-Aldasoro, G. Slabaugh, A hybrid energy model for region based curve evolution-application to cta coronary segmentation, Computer Methods and Programs in Biomedicine 144C (2017) 189–202.

[30] W. Theo, The Great Challenge, coronary artery stenoses detection and quantification evaluation framework, Available at `http://coronary.bigr.nl/stenoses/`(2016/11/11).

[31] H. Kirişli, M. Schaap, C. Metz, A. Dharampal, W. B. Meijboom, S. Papadopoulou, A. Dedic, K. Nieman, M. De Graaf, M. Meijs, et al., Standardized evaluation framework for evaluating coronary artery stenosis detection, stenosis quantification and lumen segmentation algorithms in computed tomography angiography, Medical image analysis 17 (8) (2013) 859–876.

[32] F. Renard, Y. Yang, Image analysis for detection of coronary artery soft plaques in mdct images, in: 2008 5th IEEE International Symposium on Biomedical Imaging: From Nano to Macro, 2008, pp. 25–28. `doi:10.1109/ISBI.2008.4540923`.

[33] Ponnapan, Automatic soft plaque detection from cta, Ph.D. thesis.

[34] T. F. Chan, B. Y. Sandberg, L. A. Vese, Active contours without edges for vector-valued images, Journal of Visual Communication and Image Representation 11 (2) (2000) 130–141.

[35] R. Van Uitert, I. Bitter, Subvoxel precise skeletons of volumetric data based on fast marching methods, Medical Physics 34 (2) (2007) 627–638.

[36] G. L. Raff, A. Abidov, S. Achenbach, D. S. Berman, L. M. Boxt, M. J. Bud-off, V. Cheng, T. DeFrance, J. C. Hellinger, R. P. Karlsberg, et al., Scct guidelines for the interpretation and reporting of coronary computed to-mographic angiography, Journal of Cardiovascular Computed Tomography 3 (2) (2009) 122–136.

[37] J. Dodge, B. G. Brown, E. L. Bolson, H. T. Dodge, Lumen diameter of normal human coronary arteries. influence of age, sex, anatomic variation, and left ventricular hypertrophy or dilation., Circulation 86 (1) (1992) 232–246.

[38] D. B. Darius, Coronary arteries - anatomy, Available at `http://www.heartupdate.com/anatomyfunction/coronary-arteries-anatomy_218/`(2016/11/22).

[39] K. Otsuka, S. Fukuda, A. Tanaka, K. Nakanishi, H. Taguchi, J. Yoshikawa, K. Shimada, M. Yoshiyama, Napkin-ring sign on coronary ct angiogra-phy for the prediction of acute coronary syndrome, JACC: Cardiovascular Imaging 6 (4) (2013) 448–457.

[40] P. Maurovich-Horvat, U. Hoffmann, M. Vorpahl, M. Nakano, R. Virmani, H. Alkadhi, The napkin-ring sign: Ct signature of high-risk coronary plaques?, JACC: Cardiovascular Imaging 3 (4) (2010) 440–444.

[41] H. Liu, H. Motoda, Computational Methods of Feature Selection, CRC Press, 2007.

[42] I. Guyon, J. Weston, S. Barnhill, V. Vapnik, Gene selection for cancer clas-sification using support vector machines, Machine learning 46 (1-3) (2002) 389–422.

[43] Q. Gu, Z. Li, J. Han, Generalized fisher score for feature selection, arXiv preprint arXiv:1202.3725.

[44] G. Roffo, S. Melzi, M. Cristani, Infinite feature selection, in: 2015 IEEE International Conference on Computer Vision (ICCV), 2015, pp. 4202–4210. doi:10.1109/ICCV.2015.478.